

University of Nebraska - Lincoln

DigitalCommons@University of Nebraska - Lincoln

---

Faculty Publications from the Department of  
Electrical and Computer Engineering

Electrical & Computer Engineering, Department of

---

2015

# Leveraging Nanocavity Harmonics for Control of Optical Processes in 2D Semiconductors

Gleb M. Akselrod

*Duke University*

Tian Ming

*Massachusetts Institute of Technology*

Christos Argyropoulos

*University of Nebraska-Lincoln, christos.argyropoulos@unl.edu*

Thang B. Hoang

*Duke University*

Yuxuan Lin

*Massachusetts Institute of Technology*

*See next page for additional authors*

Follow this and additional works at: <https://digitalcommons.unl.edu/electricalengineeringfacpub>



Part of the [Computer Engineering Commons](#), and the [Electrical and Computer Engineering Commons](#)

---

Akselrod, Gleb M.; Ming, Tian; Argyropoulos, Christos; Hoang, Thang B.; Lin, Yuxuan; Ling, Xi; Smith, David R.; Kong, Jing; and Mikkelsen, Maiken H., "Leveraging Nanocavity Harmonics for Control of Optical Processes in 2D Semiconductors" (2015). *Faculty Publications from the Department of Electrical and Computer Engineering*. 414.

<https://digitalcommons.unl.edu/electricalengineeringfacpub/414>

This Article is brought to you for free and open access by the Electrical & Computer Engineering, Department of at DigitalCommons@University of Nebraska - Lincoln. It has been accepted for inclusion in Faculty Publications from the Department of Electrical and Computer Engineering by an authorized administrator of DigitalCommons@University of Nebraska - Lincoln.

---

**Authors**

Gleb M. Akselrod, Tian Ming, Christos Argyropoulos, Thang B. Hoang, Yuxuan Lin, Xi Ling, David R. Smith, Jing Kong, and Maiken H. Mikkelsen

## Leveraging Nanocavity Harmonics for Control of Optical Processes in 2D Semiconductors

Gleb M. Akselrod,<sup>†,‡</sup> Tian Ming,<sup>||</sup> Christos Argyropoulos,<sup>†,‡,⊥</sup> Thang B. Hoang,<sup>†,§</sup> Yuxuan Lin,<sup>||</sup> Xi Ling,<sup>||</sup> David R. Smith,<sup>†,‡,§</sup> Jing Kong,<sup>||</sup> and Maiken H. Mikkelsen<sup>\*,†,‡,§</sup>

<sup>†</sup>Center for Metamaterials and Integrated Plasmonics, Duke University, Durham, North Carolina 27708, United States

<sup>‡</sup>Department of Electrical and Computer Engineering, Duke University, Durham, North Carolina 27708, United States

<sup>§</sup>Department of Physics, Duke University, Durham, North Carolina 27708, United States

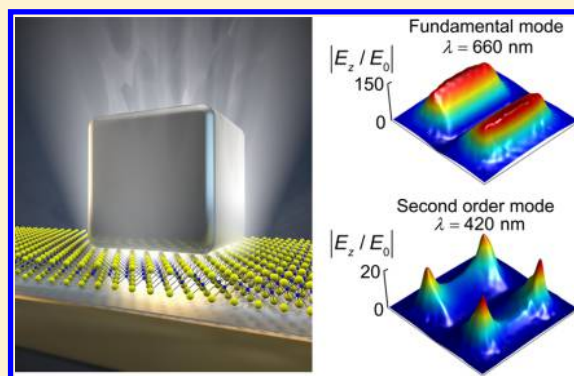
<sup>||</sup>Department of Electrical Engineering and Computer Science, Massachusetts Institute of Technology, Cambridge, Massachusetts 02139, United States

<sup>⊥</sup>Department of Electrical and Computer Engineering, University of Nebraska-Lincoln, Lincoln, Nebraska 68588, United States

### Supporting Information

**ABSTRACT:** Optical cavities with multiple tunable resonances have the potential to provide unique electromagnetic environments at two or more distinct wavelengths—critical for control of optical processes such as nonlinear generation, entangled photon generation, or photoluminescence (PL) enhancement. Here, we show a plasmonic nanocavity based on a nanopatch antenna design that has two tunable resonant modes in the visible spectrum separated by 350 nm and with line widths of  $\sim 60$  nm. The importance of utilizing two resonances simultaneously is demonstrated by integrating monolayer MoS<sub>2</sub>, a two-dimensional semiconductor, into the colloiddally synthesized nanocavities. We observe a 2000-fold enhancement in the PL intensity of MoS<sub>2</sub>—which has intrinsically low absorption and small quantum yield—at room temperature, enabled by the combination of tailored absorption enhancement at the first harmonic and PL quantum-yield enhancement at the fundamental resonance.

**KEYWORDS:** Plasmonics, nanocavity, nanocube, 2D semiconductors, MoS<sub>2</sub>, photoluminescence enhancement



Nanocavities with independently tunable harmonics are desirable for applications in which large electric field enhancements are required at two or more distinct wavelengths. For example, to efficiently generate entangled photons, an optical cavity with two spectrally separated modes could simultaneously enhance the biexciton and single-exciton transitions in a quantum emitter such as a quantum dot.<sup>1</sup> Likewise, nonlinear processes such as harmonic generation could be enhanced using cavity resonances that increase the optical fields at the fundamental frequency and at higher harmonics.<sup>2–5</sup> Other nonlinear phenomena, including stimulated Raman scattering, optical switching, and two-photon absorption, could also be enhanced in a similar manner. Furthermore, tuning and optimization of multiple resonances could be applied to fluorescent emitters, for which one cavity resonance enhances the absorption, and another resonance at the emission wavelength enhances the radiative rate and quantum efficiency via the Purcell effect.<sup>6</sup>

To achieve these effects, an optical cavity must possess two well-defined spectrally separated but spatially overlapped modes, each with a small mode volume  $V_{\text{eff}}$  and large field enhancement. At the same time, the line width of each mode

must be large enough to overlap well with broad, room-temperature emitters and the cavities must radiate efficiently into free space or into a waveguide. Dielectric cavities with multiple resonances have been demonstrated using Fabry–Pérot resonators or photonic crystal cavities.<sup>4</sup> However, these dielectric cavities rely on high quality factors ( $Q \sim 3000$ ) to achieve field enhancement, making them difficult to integrate with spectrally broad optical features ( $\sim 50$  nm), such as the absorption and photoluminescence of materials at room temperature. Additionally, for the enhancement of nonlinear effects, the narrow resonances of each individual cavity need to be precisely tuned relative to the fundamental and other generated frequencies, limiting versatility and scalability.

Plasmonic nanocavities can overcome the line width matching problem by offering spectrally broad resonances while simultaneously providing large values of  $Q/V_{\text{eff}}$ , the figure of merit that determines the rate of optical processes such as the Purcell effect.<sup>7</sup> Several designs have recently been

**Received:** March 17, 2015

**Revised:** April 13, 2015

**Published:** April 27, 2015

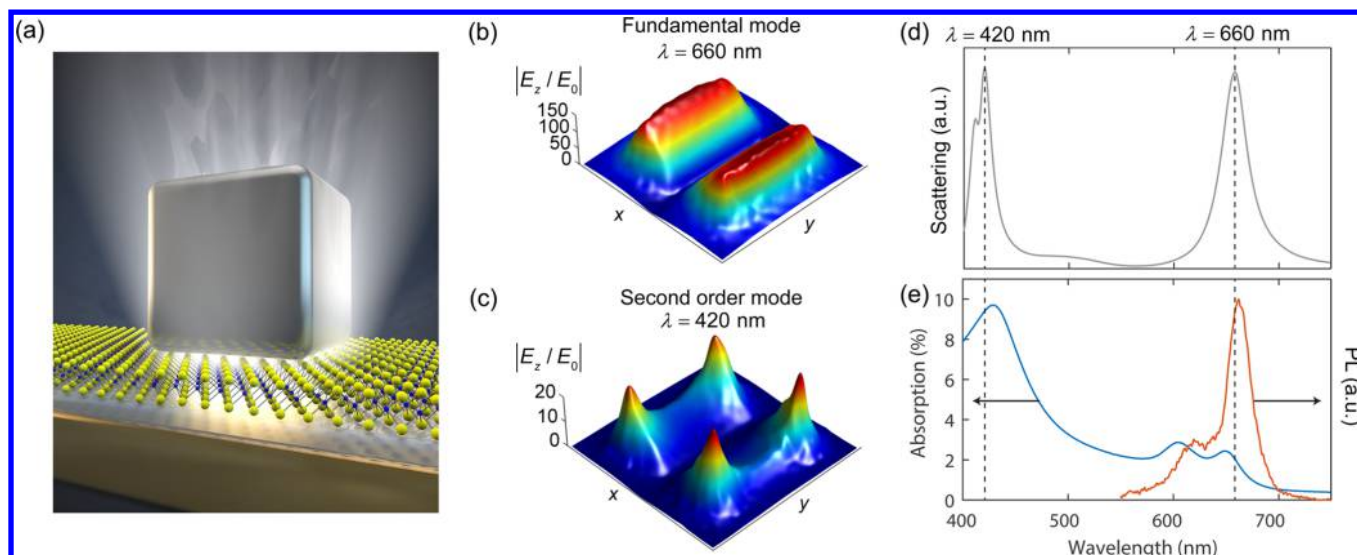


**Figure 1.** (a) 3D illustration of the nanocavity, consisting of a silver nanocube over a gold substrate, separated by a monolayer of MoS<sub>2</sub>, HfO<sub>2</sub> and polymer layers. (b–c) Spatial maps of the field enhancement across the nanocavity at (b) the fundamental-mode resonance wavelength of  $\lambda_p = 660$  nm and (c) the second-order mode resonance wavelength of  $\lambda_p = 420$  nm. (d) Simulated scattering spectrum of a nanocavity, showing the two resonances depicted in b–c. (e) Optical absorption (blue) and PL (red) spectra of monolayer MoS<sub>2</sub> on SiO<sub>2</sub>. The absorption peaks overlap well with the two nanocavity resonances, and the PL spectrum overlaps well with the fundamental resonance.

theoretically proposed for multimode plasmonic structures.<sup>8–10</sup> However, a typical plasmonic cavity such as a bowtie antenna<sup>6</sup> has only a single usable resonance. Larger plasmonic cavities can support multiple accessible modes; however, the modes are not well spectrally separated<sup>11,12</sup> or show significant overlap with each other.<sup>13</sup> Recently, a lithographically fabricated dual-resonance antenna was demonstrated to enhance second-harmonic generation, but it showed limited improvement over a single-resonance antenna.<sup>2</sup>

Here, we demonstrate a plasmonic nanocavity with ultrasmall effective mode volumes [ $V_{\text{eff}} \approx 0.001 (\lambda/n)^3$ ] and two modes separated by 350 nm across the visible spectrum with good spatial overlap (Figure 1). The nanocavity structure consists of a silver nanocube ( $\sim 75$  nm edge length) over a gold film separated by a nanoscale spacer ( $< 10$  nm), into which luminescent, nonlinear, or other materials can be integrated. The finesse of the cavity is  $F = 6$ , defined as the ratio between the mode separation and the mode line width. This high finesse plasmonic structure is enabled by the transmission line mode of the nanocavity that propagates in the gap between the two metal surfaces.<sup>14</sup>

The particular geometry is well-suited for optical control of two-dimensional materials, such as the atomic layers of MoS<sub>2</sub> that we demonstrate here. We find a dramatic 2000-fold average enhancement of the photoluminescence (PL) intensity of MoS<sub>2</sub> integrated within the nanopatch antenna. This large PL enhancement is the result of a combination of enhanced absorption at the first harmonic cavity resonance, enhanced PL quantum yield (QY) at the fundamental cavity resonance and increased directionality of the emission due to the radiation pattern of the nanopatch antenna. This nanocavity design is a particularly powerful platform for the promising transition-metal dichalcogenide monolayers,<sup>15</sup> such as MoS<sub>2</sub>, because of their intrinsically weak absorption ( $\sim 3\%$ )<sup>16</sup> combined with low PL quantum yield (0.5%).<sup>17</sup> Although other types of cavities have been used to enhance the PL of two-dimensional materials,<sup>18–23</sup> such large enhancements have not previously

been possible because both the absorption and the quantum yield could not be simultaneously enhanced.

The fundamental mode of the cavity is dipolar (Figure 1b), with a typical resonance of  $\lambda_p = 660$  nm, whereas the first harmonic is quadrupolar (Figure 1c), with a typical resonance of  $\lambda_p = 420$  nm.<sup>24</sup> The two modes are spectrally separated but also exhibit good spatial overlap. Both resonances can be observed in the scattering spectrum of the nanocavity, in simulations (Figure 1d), and in the measured white-light scattering spectrum as will be shown below. The sub-10 nm vertical dimension of the cavity results in a large electric-field enhancement ( $> 100$ ) across the gap along the  $z$  direction (Figure 1b–c) as well as weaker, but still important, field enhancement ( $\sim 10$ ) in the  $xy$  plane (Figure S1). Furthermore, our prior work has shown that the emission from the nanocavity is directional, with a single radiation lobe normal to the substrate, and with the entire structure behaving as a nanoscale patch antenna (Figure 1a).<sup>25</sup>

The large aspect ratio between the small vertical dimension ( $< 10$  nm) and the larger horizontal dimension ( $\sim 75$  nm) of the nanocavity makes it ideal for the integration of two-dimensional materials. MoS<sub>2</sub> monolayers were selected because of the good spectral overlap between the quasi-particle gap of 2.8 eV (443 nm) at the K point of MoS<sub>2</sub><sup>26</sup> and the quadrupolar mode of the nanocavity (Figure 1d–e). In addition, the fundamental nanocavity resonance overlaps with the A– trion, A exciton, and B exciton emission at approximately 1.8, 1.9, and 2.0 eV (689, 653, and 620 nm), respectively,<sup>16</sup> such that resonant enhancement of the spontaneous emission rate is possible. This alignment of the optical features allows for simultaneous enhancement of the absorption and the PL quantum yield, as will be shown below.

The nanocavity consists of a gold film (50 nm) on a glass substrate coated with 3–15 nm of HfO<sub>2</sub> (Figure 2a). MoS<sub>2</sub> is transferred onto the HfO<sub>2</sub> film, followed by deposition of colloidal silver nanocubes. The density of the deposited nanocubes was constrained to be sufficiently low to enable individual nanocavities to be addressed optically. A control

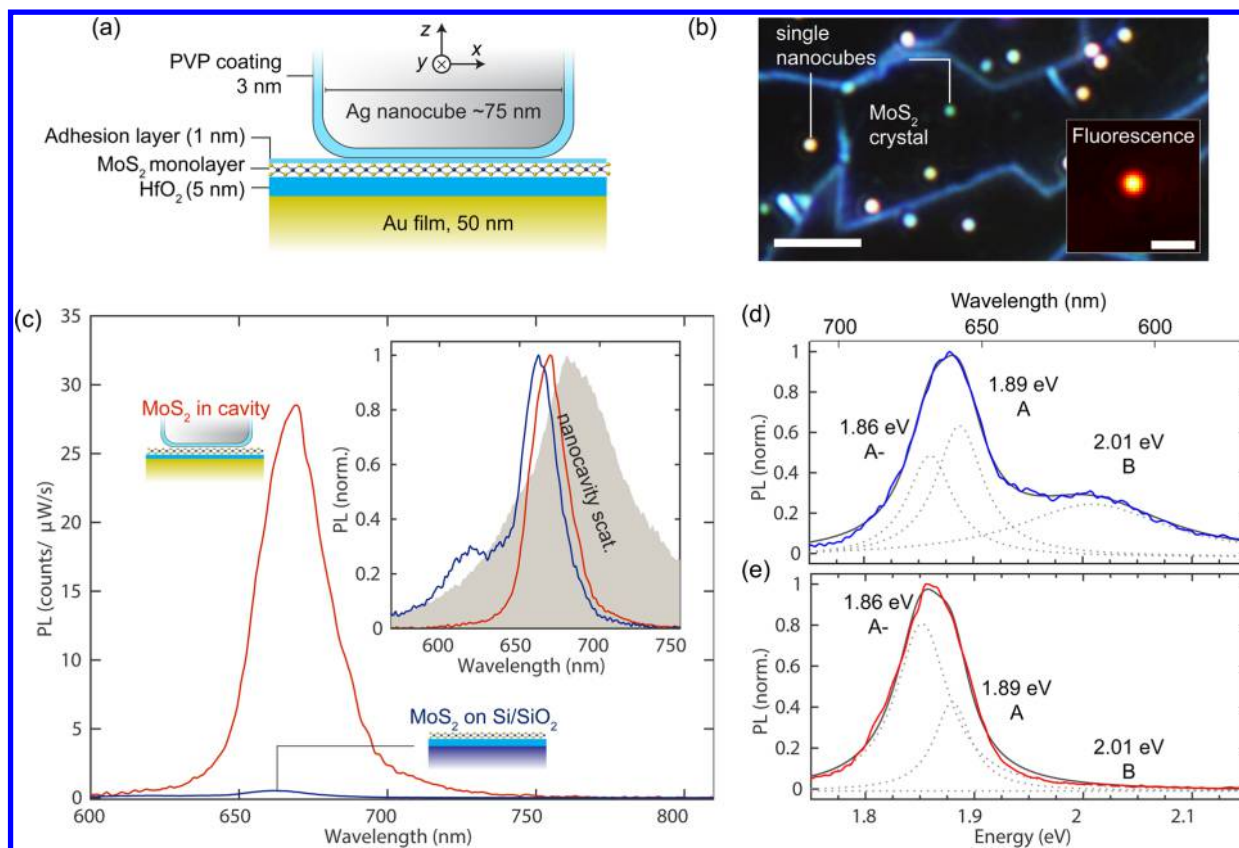


**Figure 2.** (a) Cross-sectional schematic illustration of the fabricated nanocavity samples. A gold film was coated with 5 nm of HfO<sub>2</sub>, followed by the transfer of monolayer MoS<sub>2</sub>, the deposition of a 1 nm polymer adhesion layer and the deposition of colloidal silver nanocubes. (b) Dark-field scattering image of the structure, in which the edges of the monolayer MoS<sub>2</sub> crystals appear as blue outlines and individual nanocavities appear as bright spots. The scale bar represents 5  $\mu\text{m}$ . The inset shows a PL image of a different region on the sample obtained under illumination with a defocused laser beam, showing PL from a single nanocavity (bright spot) on monolayer MoS<sub>2</sub>. The scale bar represents 1.5  $\mu\text{m}$ . (c) PL spectra from a MoS<sub>2</sub> monolayer on a SiO<sub>2</sub>/Si substrate (blue) and in the nanocavity (red) obtained using a diffraction-limited excitation spot. The intensity is measured per unit of excitation power and per unit of integration time. The inset presents normalized spectra for the two cases along with the scattering spectrum for a typical nanocavity (gray). (d and e) Normalized PL spectra from a MoS<sub>2</sub> monolayer on a SiO<sub>2</sub>/Si substrate (d) and in the nanocavity (e). The measured spectra (blue and red lines) are fitted to the A<sup>-</sup> trion and A and B exciton peaks at 1.86, 1.89, and 2.01 eV, respectively (dashed lines). The solid black lines represent the sums of the three exciton components.

sample, which consisted of a MoS<sub>2</sub> monolayer on the native substrate of Si/SiO<sub>2</sub> (290 nm), was also fabricated.

Single nanocavities can be identified by dark-field scattering microscopy, where the nanocavity scattering manifests as bright spots (Figure 2b). MoS<sub>2</sub> appears in the dark-field image as pale blue outlines because of the scattering from the edges of the crystals, which had typical dimensions of 10–20  $\mu\text{m}$ . The enhanced PL from nanocavities that are resonant with the PL spectrum are observed as bright diffraction-limited spots on a background of weak emission from the surrounding MoS<sub>2</sub> crystal (Figure 2b inset). A diffraction-limited laser spot was used to excite individual nanocavities, and the PL was collected into an imaging spectrograph or by a photon-counting avalanche photodiode.

At an excitation wavelength of  $\lambda_{\text{ex}} = 420$  nm, the single-nanocavity PL exhibits a 56-fold enhancement in intensity relative to emission from the control sample at the same excitation power (Figure 2c) and using the same diffraction-limited laser spot ( $\sim 350$  nm). The shape of the PL spectrum is also modified by the nanocavity; it is narrower and slightly ( $\sim 5$  nm) red-shifted relative to the intrinsic spectrum on the Si/SiO<sub>2</sub> substrate (Figure 2c inset). The intrinsic PL spectrum from the control sample and from the nanocavity can be well

fitted to Lorentz-shaped MoS<sub>2</sub> A<sup>-</sup> trion, A and B exciton peaks at 1.86, 1.89, and 2.01 eV, respectively (Figure 2d–e). Because the fundamental resonance for this nanocavity occurred at  $\lambda_p = 675$  nm, corresponding to a photon energy of 1.84 eV, the effect of the coupling was to skew the PL toward the cavity scattering spectrum. Alternatively, this effect could also be used to enhance weakly emitting exciton species such as the B exciton in MoS<sub>2</sub> by tuning the nanocavity resonance to 2 eV.

To reveal the effects of cavity resonances and intrinsic MoS<sub>2</sub> absorption on the PL, we examine the PL enhancement as a function of the excitation wavelength, referred to as the photoluminescence excitation (PLE) spectrum. The PLE spectrum on the control sample exhibits a peak at  $\lambda_{\text{ex}} = 610$  nm, and a dip is observed at  $\lambda_{\text{ex}} = 420$  nm. Excitation beyond 640 nm was not possible because of overlap with the PL spectrum. These features are due to the absorption of MoS<sub>2</sub> on the Si/SiO<sub>2</sub> substrate, which is modified relative to free space (Figure 3b). Using the ratio between the experimentally measured PLE spectrum and the calculated absorption, we can obtain the relative PL quantum yield,  $QY_0$ , of MoS<sub>2</sub> on thermal oxide.

The PLE spectrum of a single nanocavity with a 5 nm spacer layer reveals greatly enhanced PL intensities relative to the

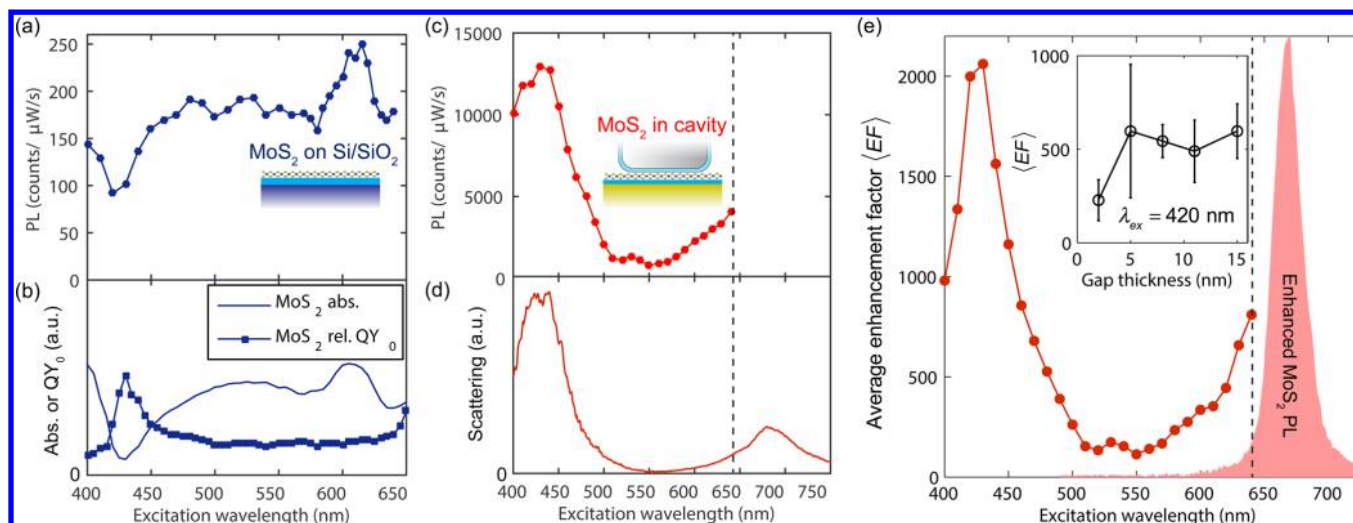


**Figure 3.** (a) Measured PL intensity as a function of excitation wavelength for the control sample consisting of a MoS<sub>2</sub> monolayer on a thermal oxide substrate. (b) Calculated absorption of MoS<sub>2</sub> on the thermal oxide substrate and the corresponding relative intrinsic PL quantum yield, QY<sub>0</sub>. (c) Measured PL intensity of MoS<sub>2</sub> coupled to a nanocavity as a function of excitation wavelength. (d) Scattering spectrum of the nanocavity measured in (c), illustrating that the PLE spectrum follows the scattering spectrum. (e) Fluorescence enhancement factor per unit area, ⟨EF⟩, for nanocavity emission relative to MoS<sub>2</sub> on thermal oxide. The inset shows ⟨EF⟩ at λ<sub>ex</sub> = 420 nm as a function of the HfO<sub>2</sub> spacer thickness (excluding the 3 nm PVP nanocube coating), based on measurements of ~6 nanocavities for each spacer thickness. The error bars represent one standard deviation.

control sample (Figure 3c). In particular, the PLE spectrum follows the nanocavity scattering spectrum, with the largest PL intensities observed near the fundamental and second-order resonances, as can be seen in the measured scattering spectrum shown in Figure 3d. To quantify the PL enhancement, we define the average PL enhancement factor across a single cavity:

$$\langle \text{EF} \rangle = \frac{I_{\text{cav}} A_0}{I_0 A_{\text{cav}}} \quad (1)$$

where  $I_{\text{cav}}$  is the PL intensity from the cavity and  $I_0$  is the PL intensity from MoS<sub>2</sub> on thermal oxide. To determine the enhancement per unit area of the MoS<sub>2</sub>, the enhancement is scaled by the ratio of the excitation area on the control sample,  $A_0 \sim (350 \text{ nm})^2$ , to the area of the nanocavity,  $A_{\text{cav}} \sim (75 \text{ nm})^2$ . Furthermore, we correct for the fact that the diffraction-limited focal spot on the sample is smaller at shorter wavelengths. The enhancement factor follows the cavity scattering spectrum, with a maximum enhancement of ⟨EF⟩ = 2000 at the second-order resonance and a value of ⟨EF⟩ = 800 as the excitation approaches the fundamental resonance at λ<sub>ex</sub> = 640 nm (Figure 3e). We note that the presence of two spectrally separated cavity resonances creates flexibility in the manner in which MoS<sub>2</sub> enhancement is achieved: large PL enhancements can be obtained through excitation near the fundamental resonance, which overlaps with the emission peak or through excitation at the second-order resonance, which overlaps with the strong MoS<sub>2</sub> absorption peak at 443 nm.

We repeated the PL enhancement measurements on samples with different HfO<sub>2</sub> spacer thicknesses, ranging from 2 to 15 nm, excluding the 3 nm PVP nanocube coating. The average enhancement factor for the ~6 selected cavities for each spacer thickness was found to have a nearly constant value of ~550 under excitation at 420 nm for spacer thicknesses of  $d = 5, 8,$  and 11 nm. For  $d = 2$  nm, ⟨EF⟩ decreases, which is attributed to nonradiative quenching.<sup>25</sup> The nanocavity on which the PLE spectrum depicted in Figure 3e was measured yielded one of the highest enhancement factors observed in our measurements. The variation from cavity to cavity could be caused by

variations in the cavity resonance relative to the PL spectrum, roughness in the gold film, or unevenness in the intrinsic PL of the MoS<sub>2</sub>.

The large PL enhancements can be understood based on full-wave finite element simulations of the nanocavity (see Methods). Figures 4a–b illustrate the relevant rates in the coupled and uncoupled MoS<sub>2</sub> monolayer, with excitation rate  $\gamma_{\text{ex}}$  and the radiative  $\gamma_r$  and nonradiative  $\gamma_{\text{nr}}$  exciton decay rates enhanced in the presence of the cavity. The intrinsic decay rate  $\gamma_{\text{int}}^0$  is assumed to be unchanged in the cavity. Because an MoS<sub>2</sub> monolayer is a two-dimensional material, it is assumed that it has an optical response only to in-plane electric fields.<sup>27</sup> Although the dominant fields in the cavity are vertical (out-of-plane), there are still substantial in-plane electric fields at both the fundamental and second-order resonances (Figure S1). Simulations of the absorption enhancement relative to free space show a dipolar pattern near the fundamental mode at λ<sub>ex</sub> = 640 nm, whereas a quadrupolar pattern is observed at the second-order mode at λ<sub>ex</sub> = 420 nm (Figure 4c). The largest enhancements are observed near the edges of the nanocube, where the in-plane fringing fields are largest because of the ~8 nm rounding of the edges, as in the experimental structure.<sup>24</sup>

The quantum yield for spontaneous emission when the MoS<sub>2</sub> is coupled to the nanocavity is given by  $\text{QY} = \gamma_r / (\gamma_r + \gamma_{\text{nr}} + \gamma_{\text{int}}^0)$  and is calculated using the dyadic Green's function (Figure 4c). The maximum local enhancement in QY is ~25 at the second order resonance. Critically, the enhancement in the QY is not strongly dependent on the intrinsic QY<sub>0</sub> of MoS<sub>2</sub>, which occurs because the quantum yield enhancement is equivalent to the radiative rate enhancement for large  $\gamma_{\text{int}}^0$ . When the effects of absorption and QY enhancement are combined, the PL enhancement factor relative to the MoS<sub>2</sub> of the control sample is

$$\text{EF}(r) = \frac{\eta \gamma_{\text{ex}}(r) \text{QY}(r)}{\eta_0 \gamma_{\text{ex}}^0 \text{QY}_0} \quad (2)$$

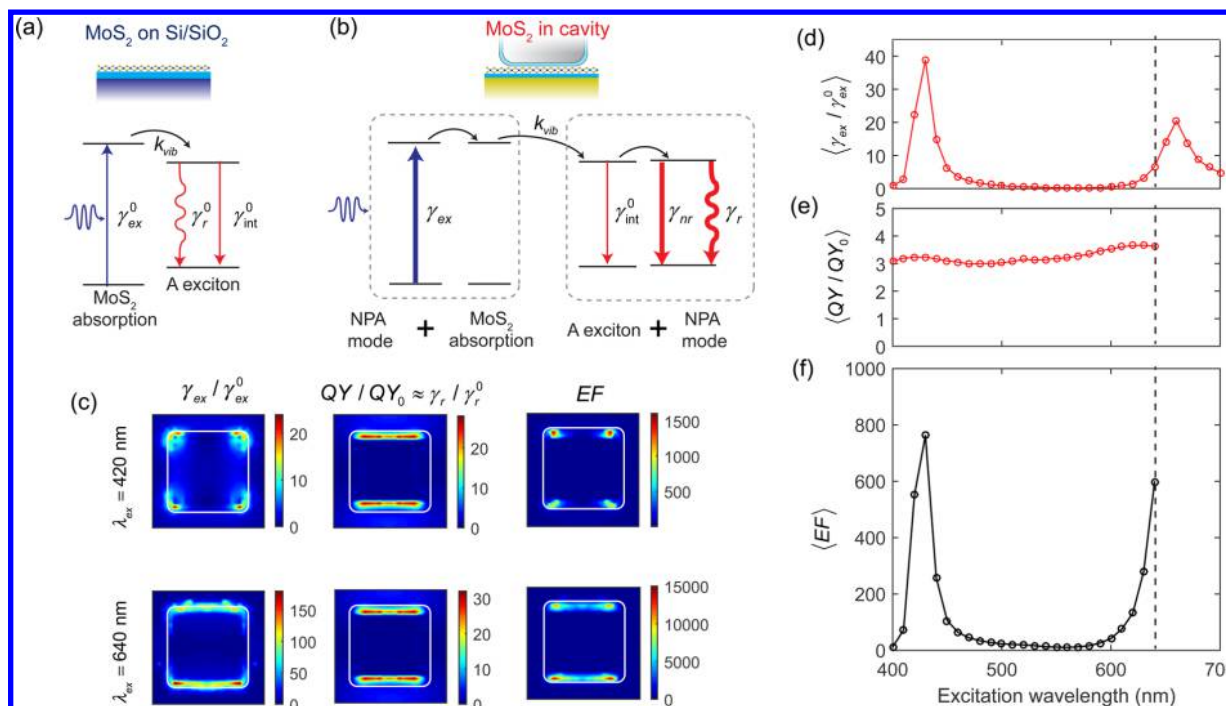


**Figure 4.** (a) Energy diagram of the absorption and emission process for MoS<sub>2</sub> on the control substrate and (b) for MoS<sub>2</sub> coupled to a nanocavity, demonstrating an enhanced absorption rate  $\gamma_{ex}$  due to coupling to the nanocavity modes and enhanced radiative  $\gamma_r$  and nonradiative  $\gamma_{nr}$  decay rates. (c) Spatial maps of the excitation rate enhancement  $\gamma_{ex}/\gamma_{ex}^0$  relative to free space, quantum-yield enhancement  $QY/QY_0$ , and enhancement factor EF for two excitation wavelengths ( $\lambda_{ex} = 420$  nm and  $\lambda_{ex} = 640$  nm) due to in-plane fields. The QY enhancement is equivalent to enhancement of the radiative rate for a small intrinsic  $QY_0$ . (d) Average excitation-rate enhancement as a function of excitation wavelength relative to MoS<sub>2</sub> on the control sample. (e) Average QY enhancement as a function of excitation wavelength. (f) Average simulated enhancement factor as a function of excitation wavelength relative to MoS<sub>2</sub> on the control substrate.

where  $\eta = 84\%$  and  $\eta_0 = 15\%$  are the PL collection efficiencies for the nanocavity sample and the Si/SiO<sub>2</sub> control sample using a 0.9 NA objective and  $QY_0$  is the intrinsic quantum yield of MoS<sub>2</sub>. The enhancement factor follows the spatial profile of the excitation rate enhancement and has a maximum value of  $\sim 1500$  at the second order resonance.

By spatially averaging the effects of enhancements in excitation and QY, we can obtain the PL enhancement factor versus the excitation wavelength (Figure 4d–f), all originating from the in-plane cavity fields. Near the fundamental resonance, the total simulated enhancement is  $\langle EF \rangle = 600$ , whereas at the second-order resonance,  $\langle EF \rangle = 800$ . For comparison of these results with the experimental enhancement factors, these enhancement factors are calculated relative to MoS<sub>2</sub> on the control substrate (Figure 4d and f). The enhancement factors (Figure 4f) exhibit good qualitative agreement with the measured enhancement factors presented in Figure 3e.

This work demonstrates a flexible and tunable plasmonic platform that possesses two spectrally separated resonances spanning the visible spectrum, which is used here to simultaneously enhance the absorption and PL quantum yield of a nanoscale material. Although the dominant vertical electric field in this nanocavity does not couple well to the horizontal dipole moment of MoS<sub>2</sub>, large enhancements are still possible due to significant in-plane and fringing fields. Strategies to improve coupling to the vertical cavity field may include introducing nanoscale roughness in the cavity or utilizing 2D semiconductor heterostructures. The resonance wavelength of the nanocavity is easily tuned by changing the nanocube size or gap thickness enabling optical processes in a wide range of materials to be enhanced from the visible to the near-

infrared.<sup>24,28</sup> Future work will focus on whether the fundamental and second-order resonance can be tuned independently such that a full frequency octave can be spanned.

The large absorption enhancement achieved in this structure could be utilized to increase the responsivity of photodetectors based on two-dimensional semiconductors. In addition, the demonstrated enhancements in PL quantum yield and directional emission could be harnessed for light-emitting diodes based on these materials. The multiresonant design of the cavity is general, such that a wide range of two-dimensional and other optically active nanoscale materials can be integrated for the enhancement of photoluminescence, absorption, nonlinear effects, and other processes. In addition, by increasing the nanocube density, the collective effects of neighboring nanocavities can be harnessed to further increase the optical response. Moreover, the absorption and quantum-yield enhancements, as well as yet-to-be-utilized effects, of these cavities can be achieved over macroscopic areas because of the colloidal fabrication technique.<sup>28</sup>

**Methods. Sample Fabrication.** First, 50 nm gold films were prepared via electron beam evaporation at a rate of 1 Å/s onto clean glass slides coated with a 5 nm adhesion layer of evaporated Ti. Next, HfO<sub>2</sub> spacer layers were deposited on the gold films via atomic layer deposition (ALD), using tetrakis dimethylamido-hafnium and deionized (DI) water as precursors at a temperature of 250 °C. HfO<sub>2</sub> film thicknesses of 2, 5, 8, 11, and 15 nm were realized by performing 25, 63, 100, 138, and 188 cycles of ALD, respectively.

Monolayer MoS<sub>2</sub> was synthesized using the seeding-promoter-assisted CVD method.<sup>29</sup> In brief, molybdenum trioxide (MoO<sub>3</sub>) and sulfur (S) were used as precursors and

were loaded into two separated crucibles. At a growth temperature of 650 °C, MoO<sub>3</sub> and S react to form MoS<sub>2</sub>. A 300 nm SiO<sub>2</sub>/Si substrate, on which the seeding promoter perylene-3,4,9,10-tetracarboxylic acid tetrapotassium salt (PTAS) was loaded, was placed face down on the crucible together with MoO<sub>3</sub>. The MoS<sub>2</sub> was nucleated with the assistance of the PTAS, and monolayer MoS<sub>2</sub> flakes were obtained on the substrate. The monolayer MoS<sub>2</sub> was then transferred to the HfO<sub>2</sub>-coated gold films using a polydimethylsiloxane stamping method.<sup>30</sup> The MoS<sub>2</sub> crystals were confirmed to be monolayers before and after transfer using Raman spectroscopy (Figure S3). Then, 2 μL of DI water was drop casted onto a 2 mm thick PDMS stamp, and the droplet was pressed against the MoS<sub>2</sub> on the growth substrate. Next, the PDMS stamp was peeled off with the MoS<sub>2</sub> attached and was subsequently pressed against the HfO<sub>2</sub>-coated gold film. After the PDMS was peeled off, the monolayer MoS<sub>2</sub> was left behind on the top surface of the HfO<sub>2</sub>. A polymer adhesion layer was grown by depositing a 10 μL droplet of cationic poly(allylamine) hydrochloride (PAH) (3 mM) onto a region of the substrate that contained MoS<sub>2</sub> crystals. After 5 min, the droplet was removed using nitrogen gas, followed by several washes with 10 μL water droplets. Small droplets were used to avoid submerging the sample, as submersion may cause MoS<sub>2</sub> to delaminate from its substrate.

Colloidal silver nanocubes were synthesized using a previously described method.<sup>28</sup> After a 100-fold dilution, a 10 μL droplet of the nanocube solution was deposited onto the region coated with PAH, to which the nanocubes adhered. After 5 min, the nanocube droplet was removed with nitrogen gas, and the area was washed with water droplets.

**Optical Measurements.** Measurements were performed using a custom-built optical microscope (Figure S2). Nanocavities and MoS<sub>2</sub> were identified via dark-field illumination imaging using a 0.9 NA dark-field objective lens. The light scattered from the nanocavities was imaged through an intermediate pinhole aperture onto an imaging spectrograph to obtain the scattering spectrum and identify the resonance wavelength. For PL measurements, the excitation source was a Ti:sapphire laser with an 80 MHz repetition rate and a 150 fs pulse length, which pumped an optical parametric oscillator (OPO) to produce wavelengths from 400 to 640 nm. The output of the OPO was then coupled to a single-mode fiber. The collimated fiber output was passed through a defocusing lens and then imaged onto the sample plane, creating a ~20 μm spot. We then selected only cavities that both exhibited PL under this widefield excitation and simultaneously possessed a resonance at ~660 nm, as determined from the dark-field measurements. For quantitative PL measurements, the defocusing lens was removed, and the laser was focused to a diffraction-limited spot on the nanocavity. Monolayer MoS<sub>2</sub> on gold in areas far from the nanocavity exhibits very weak PL and contributes <10% of the total PL signal. The PL was collected by the objective, passed through a 647 nm long-pass fluorescence filter and detected by a single-photon-counting avalanche photodiode (50 μm active area, Micro Photon Devices) connected to a counting module (PicoHarp 300, Picoquant Inc.). Every time the excitation wavelength was changed, the fiber output was recollimated to ensure that the laser focal spot and avalanche photodiode remained confocal.

**Simulations.** We used three-dimensional (3D) finite-element simulations (COMSOL Multiphysics) to calculate the scattering signature of the plasmonic nanocavity, as shown

in Figure 1d. For all scattering calculations, we used a plane wave to excite the nanocavity at normal incidence. The scattered-field formalism, in which the analytical solution for an incident plane wave in the absence of the metallic nanocube is used as the background field, was employed in all 3D scattering simulations. The various components of the electric field induced at the nanogap for both excitation wavelengths (420 and 640 nm) and both nanocavity resonances (420 and 660 nm) were computed. The in-plane electric field components were  $E_x$  and  $E_y$ , and the out-of-plane component was  $E_z$ . The absorption of MoS<sub>2</sub> on the thermal oxide substrate (control sample) and the relative intrinsic PL quantum yield,  $QY_0$ , that are shown in Figure 3b were calculated using two-dimensional (2D) simulations. An infinite film of MoS<sub>2</sub> on a thermal oxide substrate was assumed, with optical constants obtained from Li et al.<sup>26</sup> The control sample was excited by a plane wave impinging at normal incidence, and the power absorbed in the MoS<sub>2</sub> was computed. The refractive index of the silica was assumed to be dispersionless and equal to  $n = 1.46$ .

The radiative, nonradiative, and total spontaneous emission rates of the plasmonic nanocavity with embedded MoS<sub>2</sub> were computed using a previously presented numerical technique.<sup>14</sup> We placed an array of monochromatic point dipoles at the gap of the nanocavity; these dipoles were emitting at both excitation wavelengths, 420 nm and 640 nm. The Green's function of the system was evaluated by varying the position of each dipole emitter on a discrete 15 × 15 grid in the gap. Based on these calculations, we theoretically computed the local density of states, the total spontaneous decay rate, and the radiative quantum efficiency of the experimentally investigated plasmonic/MoS<sub>2</sub> structure.

## ■ ASSOCIATED CONTENT

### 📄 Supporting Information

Simulations of electric field enhancement in the cavity, diagram of experimental setup, and characterization of MoS<sub>2</sub> monolayers. The Supporting Information is available free of charge on the ACS Publications website at DOI: 10.1021/acs.nanolett.5b01062.

## ■ AUTHOR INFORMATION

### Corresponding Author

\*E-mail: m.mikkelsen@duke.edu.

### Author Contributions

G.M.A., T.M., and M.H.M. conceived and designed the experiments. G.M.A. fabricated the nanocavities, constructed the experimental setup, performed the measurements, and analyzed the data. T.M. synthesized and transferred the MoS<sub>2</sub> films. C.A. and G.M.A. performed the simulations. T.B.H. synthesized the silver nanocubes. Y.L. deposited the ALD films. X.L. guided the MoS<sub>2</sub> synthesis and preparation. G.M.A. and M.H.M. wrote the manuscript, with input from the coauthors. M.H.M., J.K., and D.R.S. supervised the project.

### Notes

The authors declare no competing financial interest.

## ■ ACKNOWLEDGMENTS

The authors thank Parag Deotare for insightful discussions. G.M.A., T.B.H., and M.H.M. acknowledge support from a Ralph E. Powe Junior Faculty Enhancement Award, the Lord Foundation of North Carolina, and the AFOSR. G.M.A. acknowledges support from the Intelligence Community



Postdoctoral Research Fellowship Program. C.A. and D.R.S. acknowledge support from the Air Force Office of Scientific Research (AFOSR, Grant No. FA9550-12-1-0491). This research was supported as part of the Center for Excitonics, an Energy Frontier Research Center funded by the U.S. Department of Energy, Office of Science, Basic Energy Sciences (BES), under award number DE-SC0001088. T.M. and J.K. acknowledge support from DOE BES Grant No. DE-SC0001088 (experimental design, MoS<sub>2</sub> synthesis, data analysis, and manuscript writing).

## REFERENCES

- (1) Benson, O.; Santori, C.; Pelton, M.; Yamamoto, Y. *Phys. Rev. Lett.* **2000**, *84*, 2513–2516.
- (2) Thyagarajan, K.; Rivier, S.; Lovera, A.; Martin, O. J. F. *Opt. Express* **2012**, *20*, 12860.
- (3) Rodriguez, A.; Soljacic, M.; Joannopoulos, J. D.; Johnson, S. G. *Opt. Express* **2007**, *15*, 7303–7318.
- (4) Buckley, S.; Radulaski, M.; Zhang, J. L.; Petykiewicz, J.; Biermann, K.; Vučković, J. *Opt. Lett.* **2014**, *39*, 5673–5676.
- (5) Lee, J.; Tymchenko, M.; Argyropoulos, C.; Chen, P.-Y.; Lu, F.; Demmerle, F.; Boehm, G.; Amann, M.-C.; Alu, A.; Belkin, M. A. *Nature* **2014**, *511*, 65–69.
- (6) Kinkhabwala, A.; Yu, Z.; Fan, S.; Avlasevich, Y.; Mullen, K.; Moerner, W. *Nat. Photonics* **2009**, *3*, 654–657.
- (7) Kavokin, A.; Baumberg, J. J.; Malpuech, G.; Laussy, F. P. *Microcavities*; Series on Semiconductor Science and Technology; OUP Oxford: Oxford, 2011.
- (8) Giannini, V.; Sánchez-Gil, J. A. *Opt. Lett.* **2008**, *33*, 899–901.
- (9) Hao, F.; Nehl, C. L.; Hafner, J. H.; Nordlander, P. *Nano Lett.* **2007**, *7*, 729–732.
- (10) Zhang, Y.; Jia, T. Q.; Zhang, S. A.; Feng, D. H.; Xu, Z. Z. *Opt. Express* **2012**, *20*, 2924.
- (11) Russell, K.; Liu, T.; Cui, S.; Hu, E. *Nat. Photonics* **2012**, *6*, 459–462.
- (12) Fan, J.; Wu, C.; Bao, K.; Bao, J.; Bardhan, R. *Science* **2010**, *210*, 1135–1138.
- (13) Yin, J.; Zang, Y.; Xu, B.; Li, S.; Kang, J.; Fang, Y.; Wu, Z.; Li, J. *Nanoscale* **2014**, *6*, 3934–3940.
- (14) Ciraci, C.; Rose, A.; Argyropoulos, C.; Smith, D. J. *Opt. Soc. Am. B* **2014**, *31*, 2601–2607.
- (15) Wang, Q. H.; Kalantar-Zadeh, K.; Kis, A.; Coleman, J. N.; Strano, M. S. *Nat. Nanotechnol.* **2012**, *7*, 699–712.
- (16) Mak, K.; He, K.; Lee, C.; Lee, G.; Hone, J. *Nat. Mater.* **2013**, *12*, 207–211.
- (17) Mak, K. F.; Lee, C.; Hone, J.; Shan, J.; Heinz, T. F. *Phys. Rev. Lett.* **2010**, *105*, 136805.
- (18) Wu, S.; Buckley, S.; Jones, A. M.; Ross, J. S.; Ghimire, N. J.; Yan, J.; Mandrus, D. G.; Yao, W.; Hatami, F.; Vučković, J.; Majumdar, A.; Xu, X. *2D Mater.* **2014**, *1*, 011001.
- (19) Gan, X.; Gao, Y.; Fai Mak, K.; Yao, X.; Shiue, R.-J.; van der Zande, A.; Trusheim, M. E.; Hatami, F.; Heinz, T. F.; Hone, J.; Englund, D. *Appl. Phys. Lett.* **2013**, *103*, 181119.
- (20) Lin, J.; Li, H.; Zhang, H.; Chen, W. *Appl. Phys. Lett.* **2013**, *102*, 203109.
- (21) Sobhani, A.; Lauchner, A.; Najmaei, S.; Ayala-Orozco, C.; Wen, F.; Lou, J.; Halas, N. J. *Appl. Phys. Lett.* **2014**, *104*, 031112.
- (22) Goodfellow, K.; Beams, R.; Chakraborty, C.; Novotny, L.; Vamivakas, A. *Optica* **2014**, *1*, 149–152.
- (23) Najmaei, S.; Mlayah, A.; Arbouet, A.; Girard, C.; Léotin, J.; Lou, J. *ACS Nano* **2014**, *8*, 12682–12689.
- (24) Lassiter, J. B.; McGuire, F.; Mock, J. J.; Ciraci, C.; Hill, R. T.; Wiley, B. J.; Chilkoti, A.; Smith, D. R. *Nano Lett.* **2013**, *13*, 5866–5872.
- (25) Akselrod, G. M.; Argyropoulos, C.; Hoang, T. B.; Ciraci, C.; Fang, C.; Huang, J.; Smith, D. R.; Mikkelsen, M. H. *Nat. Photonics* **2014**, *8*, 835–840.
- (26) Li, W.; Birdwell, A.; Amani, M.; Burke, R.; Ling, X.; Lee, Y.-H. *Phys. Rev. B* **2014**, *90*, 195434.
- (27) Schuller, J. a.; Karaveli, S.; Schiros, T.; He, K.; Yang, S.; Kymissis, I.; Shan, J.; Zia, R. *Nat. Nanotechnol.* **2013**, *8*, 271–276.
- (28) Moreau, A.; Ciraci, C.; Mock, J. J.; Hill, R. T.; Wang, Q.; Wiley, B. J.; Chilkoti, A.; Smith, D. R. *Nature* **2012**, *492*, 86–89.
- (29) Ling, X.; Lee, Y.; Lin, Y.; Fang, W. *Nano Lett.* **2014**, *14*, 464–472.
- (30) Lee, Y.; Yu, L.; Wang, H.; Fang, W.; Ling, X. *Nano Lett.* **2013**, *13*, 1852–1857.